Estimation With Threshold Sensing for Gyroscope Calibration Using a Piezoelectric Microstage

Biju Edamana, Yi Chen, Daniel Slavin, Ethem Erkan Aktakka, *Member, IEEE*, and Kenn R. Oldham, *Member, IEEE*

***Abstract*— A sensing estimation scheme is presented that combines analog and threshold sensing on a piezoelectric microactuator for calibration of microscale inertial sensors. Using a variation of the Kalman filter, an asynchronous threshold sensor improves state estimates obtained from less reliable analog sensor measurements of microactuator motion. The resulting velocity estimates are compared with estimates without threshold sensing, and related to feasible calibration performance for gyroscopes. Results show that incorporating threshold sensors in a projected low-noise environment based on capacitive sensing will produce high-accuracy velocity measurements at certain fixed angles, with an approximately 80% reduction in angular velocity estimation error. Experimental testing with noisier, more variable piezoelectric sensing shows improved estimation accuracy at all velocities and positions when threshold detections are added. In simulation, the addition of feedback control is shown to further improve estimation accuracy.**

***Index Terms*— Calibration, estimation, inertial sensing, Kalman filters, microactuators, piezoelectric actuators.**

I. Introduction

THIS brief describes an estimation scheme combining analog and threshold sensing to perform high-accuracy velocity estimation for a piezoelectric microactuator, for use in on-chip microelectromechanical system (MEMS) gyroscope calibration. MEMS gyroscopes have demonstrated excellent sensitivities, good linearity, and reasonable noise characteristics in a number of small low-power form factors. However, long-term gain and bias drift [1] are large, on the order of 10 000 ppm or more. This prevents use in long-term, inertial-grade applications, such as navigation, where accuracies of 100 ppm or better are required [2]. As a result, various calibration methods have been proposed for MEMS gyroscopes. One approach to such calibration is to carefully model inertial measurement unit (IMU) sensitivity to factors, such as temperature, humidity, and other operational parameters, and use a model to predict gain and bias changes, possibly with additional use of higher order or nonlinear dynamic behavior. Gyroscope gain accuracies on the order of a few hundred parts per million have been demonstrated by self-calibration using temperature [3] or self-excited coriolis forcing [4]. These approaches require minimal change to gyroscope hardware, but any given model of such detail is limited to a specific sensor design.

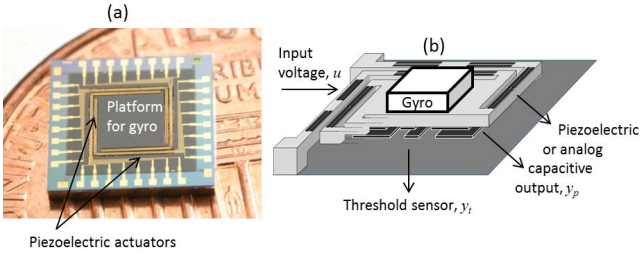

Fig. 1. (a) Piezoelectric microstage prototype to be used in gyroscope calibration. (b) Actuator input and output signals.

For more general calibration of an arbitrary MEMS gyroscope, some external stimulus must be applied. In a laboratory setting, a rate table can provide various well-defined angular rates, sometimes known as continuous calibration, or angular positions, known as multiposition calibration, to a gyroscope [5], [6]. Various methods have been proposed for extending such methods to field calibration. For continuous calibration, Kalman filtering techniques [2] and genetic algorithms [7] have been proposed to compensate for uncertainty about stimulus and frames of reference from a moving vehicle or gimbal, respectively. For multiposition calibration, which is more often proposed, a variety of techniques have been proposed for choosing inertial sensor orientations and reference stimuli and addressing uncertainties [8], [9]. However, neither the long duration velocity stimulus nor the large rotational displacements required by the above methods are easily achieved by a self-contained microsystem, and calibration duration is generally long, on the order of several minutes to an hour. Furthermore, fully realized experimental results are still limited, with calibration accuracies typically on the order of 1000 ppm.

This brief proposes a novel sensor configuration and associated estimation scheme for a piezoelectric microactuator that would allow the actuator to approach some functionalities of a rate table. As a variety of commercial or research-grade gyroscopes could be assembled to the piezoelectric actuator,

Manuscript received August 7, 2014; accepted November 9, 2014. Manuscript received in final form December 1, 2014. This work was supported by the Defense Advanced Research Projects Agency under Grant W31P4Q-12-1-0002. Recommended by Associate Editor A. Zolotas.

B. Edamana, Y. Chen, and D. Slavin are with the Department of Mechanical Engineering, University of Michigan, Ann Arbor, MI 48109 USA (e-mail: bij@umich.edu; davidsky@umich.edu; dfslavin@umich.edu).

E. E. Aktakka is with the Department of Electrical Engineering and Computer Science, University of Michigan, Ann Arbor, MI 48109 USA (e-mail: aktakka@umich.edu).

K. R. Oldham is with the Department of Mechanical Engineering, University of Michigan, Ann Arbor, MI 48109 USA (e-mail: oldham@umich.edu).

Color versions of one or more of the figures in this paper are available online at http://ieeexplore.ieee.org.

Digital Object Identifier 10.1109/TCST.2014.2386776

this approach potentially adds complexity to an inertial measurement system, but the resulting calibration system could potentially be applied to a wide variety of MEMS inertial sensors. The piezoelectric actuator, shown in Fig. 1(a), is capable of applying 3-axis translation and 3-axis rotation to a gyroscope or accelerometer payload. It is an advanced version of an actuator developed by Aktakka *et al.* [10]. If an IMU is mounted on the central platform of the actuator, precise estimates of motion applied to the IMU would not only generate calibration curves, but would also allow identification of cross-axis sensitivity, though the present work examines only motion estimation in a single axis.

The sensing and estimation scheme described in this brief attempts to address the critical challenge of measuring piezoelectric stage motion with sufficiently high accuracy to perform gyroscope calibration. As most on-chip MEMS sensors, such as capacitive, piezoelectric, or piezoresistive sensing elements, are subject to the same sources of drift as MEMS gyroscopes, they may not in general be reliable for improving gyroscope performance. Addition of high-precision threshold sensors that indicate specific piezoelectric actuator positions with exceptionally high accuracy, though they are unable to provide other positioning information, is explored as a solution to this problem. The associated estimation scheme revises a Kalman filter at threshold sensing events to improve estimates from analog capacitive or piezoelectric sensors. The theoretical approach is inspired by Astrom [11], who used a Kalman filter in an *ad hoc* estimation scheme when a sensing event occurred, though the current work derives the modified Kalman filter implementation specifically for discrete time implementation with potentially limited sampling rates, which have significant influence on estimator performance. Related approaches have also treated threshold sensor measurements as discrete events [12], [13]. An alternate approach is to assume the sensor noise to be state dependent [14], [15], but this does not effectively reflect knowledge available from the proposed on-chip sensors, while the authors have previously examined piezoelectric actuator control with a small number of analog sensor measurements in [16], but these measurements occurred at fixed times in the sampling process.

II. System Description

Over the period of time in which a proposed calibration takes place, the system to be controlled is taken to have linear, time-invariant dynamics, discretized at sampling rate T_s

$$\mathbf{x}_p(k+1) = \mathbf{A}_p\mathbf{x}_p(k) + \mathbf{B}_p u(k) + \mathbf{B}_w(w(k) + d(k)) \quad (1)$$

where $\mathbf{x}$ is system state vector and $\mathbf{A_p}$ and $\mathbf{B_p}$ are state and input matrices, respectively. It is assumed that both random, w and periodic, d, disturbances are present, acting through matrix $\mathbf{B}_w$. Random disturbance $w(k)$ is assumed to be zero-mean, white, and Gaussian with covariance matrix $\mathbf{Q}$. For the operating environment of the target piezoelectric calibration stage, $d(k)$ is taken to be an unknown periodic disturbance within a bounded frequency range and amplitude.

The specific multidegree-of-freedom piezoelectric microactuator being studied is nominally modeled as six uncoupled linear systems, corresponding to the underdamped motion in each of the six axes of motion (three translation and three rotation), its first six vibration modes. For the purposes of evaluating estimator design, a single degree of freedom is regulated and modeled as a second-order, underdamped linear system.

Due to the use of piezoelectric actuation in the target microactuator, there is mild hysteresis in the input, $u(k)$. While this is not explicitly considered during estimator design, a hysteresis model was implemented for simulations studies, converting a nominal control input u_{nom}, into

$$u(k) = u_{\text{nom}}(k) + \text{sign}(\dot{u}_{\text{nom}})\delta u \quad (2)$$

where δu is a hysteresis offset. This is not intended to be a rigorous description of hysteresis, but to ensure that a perturbation of comparable size is present during simulation studies.

A. Sensing Signals

The system is assumed to have two sensor signals available for use in position and velocity estimation, both of which are linear functions of the states. The first signal is an analog sensor available at all controller sampling times

$$y_p = \mathbf{C}_p\mathbf{x}_p + \upsilon \quad (3)$$

where $\mathbf{C}_p$ is an output matrix in state-space form and υ is white, random, Gaussian sensor noise with variance R.

In the piezoelectric microstage, the most practical sources of this signal are piezoelectric sensing from the actuator legs, used in the prototype system, or capacitive sensing from electrodes on the bottom surface of the actuator and the surface underneath. $\mathbf{C_p}$ is assumed to be imperfectly known, as there may be scale errors due to factors such as temperature change.

The second sensor is a threshold sensor that indicates the time at which a specific measure of system states (typically a specific position) occurs. This event is taken to be recorded using a clock operating N times faster than the sampling time for control at period T_t, or

$$T_t = \frac{T_s}{N}. \quad (4)$$

The threshold sensor output measure, y_t, is a linear combination of the states described by output matrix $\mathbf{C}_t$

$$y_t = \mathbf{C}_t\mathbf{x}_p \quad (5)$$

that experiences a threshold detection event when crossing a known threshold level, y_{t0}. $\mathbf{C}_t$ may or may not be the same measure of the states as produces continuous output y_p. If a threshold crossing is detected during the N clock timer increments between two measurements of continuous output y_p, the threshold crossing time, $n_t \in (0, N)$, is recorded. For example, for y_t increasing n_t is defined by

$$y_t(n_t - 1) \leq y_{t0} < y_t(n_t). \quad (6)$$

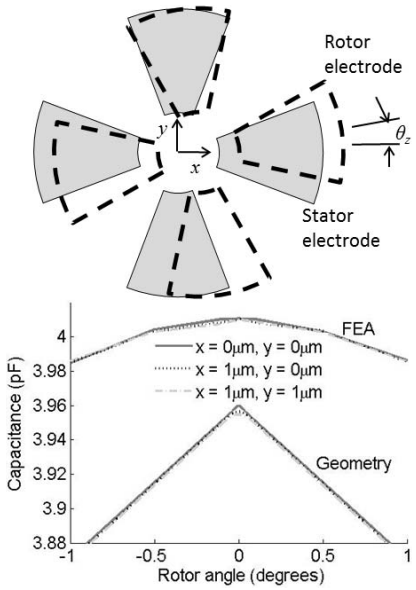

Fig. 2. Symmetric capacitive sensing electrodes (top) generate stable peak capacitance values even in the presence of nonideal off-axis motion or sensor gain errors, as shown in geometric and FEA of a sample electrode geometry (bottom).

The threshold crossing location is taken to be perfectly known, unlike the gains in the system. This may be achieved, for example, by detecting peak capacitance between sets of electrodes that are symmetric about the center of the microstage in rotation. One such electrode geometry is shown in Fig. 2, which shows capacitance versus angle for a symmetric array of electrode sectors as calculated from geometric and finite element analysis (FEA) models. At the critical angle (for the design shown in Fig. 2, 0°), electrodes overlap perfectly, and the capacitance reaches a maximum value. This occurs in both an ideal geometric model and when accounting for fringe field effects in FEA, though fringe effects reduce capacitance sensitivity. While absolute capacitance may vary with environmental changes, the location of the maximum is insensitive both to changes in the gap between electrodes and, due to symmetry, to off-axis motions such as tilt. In such a sensing scheme, threshold events are also available for crossings during decreasing y_t, and multiple sensors can be used to detect multiple threshold crossings. The only information required by the estimation algorithms is that when the threshold value is crossed, the value for n_t recorded is assumed to correspond exactly to the time at which $y_t(t) = y_{t0}$. In other words, threshold sensing is performed in open loop with an accuracy equal to the resolution of the clock.

III. Estimator Design

A. Sensing Strategy 1 (Kalman Filter Without Threshold Sensor)

Three strategies are compared for estimating the states of the system. In the first strategy, an analog position sensor alone is used. States are estimated based on noisy measurements from the sensor using a standard Kalman filter

$$\hat{\mathbf{x}}_p(k+1) = \mathbf{A}_p\hat{\mathbf{x}}_c(k) + \mathbf{B}_p u(k) \tag{7}$$

$$\mathbf{P}(k+1) = \mathbf{A}_p\mathbf{Z}(k)\mathbf{A}_p' + \mathbf{B}_p\mathbf{Q}\mathbf{B}_p' \tag{8}$$

$$\begin{aligned}\hat{\mathbf{x}}_c(k+1) = {} & \hat{\mathbf{x}}_p(k+1) - \mathbf{P}(k+1)\mathbf{C}_p'(\mathbf{C}_p\mathbf{P}(k+1)\mathbf{C}_p'+\mathbf{R})^{-1} \\ & \times(\mathbf{C}_p\hat{\mathbf{x}}_p(k+1) - \mathbf{C}_p\hat{\mathbf{x}}_p(k+1)+v(k+1))\end{aligned} \tag{9}$$

$$\begin{aligned}\mathbf{Z}(k+1) = {} & \mathbf{P}(k+1) - \mathbf{P}(k+1)\mathbf{C}_p'(\mathbf{C}_p\mathbf{P}(k+1) \\ & \times\mathbf{C}_p'+\mathbf{R})^{-1}C_p P(k+1)\end{aligned}$$

with $\hat{\mathbf{x}}$ indicating *a priori* state estimates, $\hat{\mathbf{x}}_c$ indicating *a posteriori* corrected state estimates, and $\mathbf{P}$ and $\mathbf{Z}$ being *a priori* and *a posteriori* error covariance matrices.

B. Sensing Strategy 2 (Kalman Filter With Threshold Sensor)

In the second strategy, both an analog sensor and one or more threshold sensors are considered to be available. States are estimated using Kalman filter equations based on measurements of y_p at all sampling instants as in (7). At sampling instants just after threshold sensor crossings, state estimates are modified by inserting an additional time step into the Kalman filter between the original sampling instants.

Consider a sample period in which a threshold crossing is detected. Let k^- denote the slow-sampled time step before the crossing is detected, k^+ denote the time step after the crossing is detected, and k_t denote the new time step occurring at the threshold detection, or

$$k^- < k_t = \frac{k^- + n_t}{N < k^+}. \tag{10}$$

In this notation, though k_t is not an integer, it serves to mark a discrete time point between the ordinary sampling instants.

Then, let A^- and B^- be the dynamic state matrices of the system discretized with a sampling time equal to the time between k^- and the threshold detection, $T_t n_t$, and A^+ and B^+ be the dynamics matrices of the system discretized with a sampling time of the remainder of the standard sampling period, $T_s - T_t n_t$. Using these matrices, state estimation $\hat{\mathbf{x}}(k_t)$ and covariance $\mathbf{P}(k_t)$ at the threshold crossing time is

$$\hat{\mathbf{x}}(k_t) = \mathbf{A}^-\hat{\mathbf{x}}_c(k^-) + \mathbf{A}^- u(k^-) \tag{11}$$

$$\mathbf{P}(k_t) = \mathbf{A}^-\mathbf{Z}(k^-)\mathbf{A}^{-\prime} + \mathbf{B}^-\mathbf{Q}\mathbf{B}^{-\prime}. \tag{12}$$

Using the threshold level y_{t0} in (7) are modified to obtain a posteriori estimates at k_t, $\hat{\mathbf{x}}_c(k_t)$ and $\mathbf{Z}(k_t)$

$$\hat{\mathbf{x}}_c(k_t) = \hat{\mathbf{x}}(k_t) + \mathbf{P}(k_t)\mathbf{C}_p'[\mathbf{C}_p\mathbf{P}(k_t)\mathbf{C}_p']^{-1}(y_{t0} - \mathbf{C}_p\hat{\mathbf{x}}(k_t)) \tag{13}$$

$$\mathbf{Z}(k_t) = \mathbf{P}(k_t)\mathbf{C}_p'[\mathbf{C}_p\mathbf{P}(k_t)\mathbf{C}_p']^{-1}\mathbf{C}_p\mathbf{P}(k_t). \tag{14}$$

After obtaining a posteriori estimates at the threshold crossing time, these estimates can be used to obtain its *a priori* estimates for the k^+ time step

$$\hat{\mathbf{x}}_p(k^+) = \mathbf{A}^+\hat{\mathbf{x}}_c(k_t) + \mathbf{B}^+\mathbf{u}(k^-) \tag{15}$$

$$\mathbf{P}(k^+) = \mathbf{A}^+\mathbf{Z}(k_t)\mathbf{A}^{+\prime} + \mathbf{B}^+\mathbf{Q}\mathbf{B}^{+\prime}. \tag{16}$$

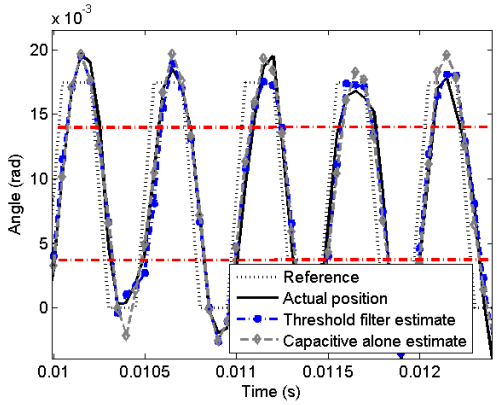

Fig. 3. Sample time response showing reference trajectory, actual trajectory, state estimation based on analog sensing alone, and estimates with threshold sensing.

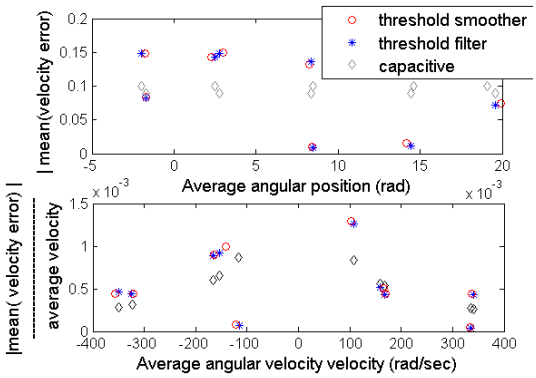

Fig. 4. With two threshold sensors, at least two angular velocity estimates are found to dramatically improve, both in absolute error (top plot, versus position) and in relative error (bottom plot, versus velocity).

C. Sensing Strategy 3 (Smoother With Threshold Sensor)

During calibration tasks, the entire time series of data may be stored to improve state estimates using a Kalman smoother. At the end of each reference period, the last threshold crossing time is determined. Using the state estimates from the threshold crossing time, estimates of the previous states were improved using Kalman smoother equations (17) according to

$$\hat{\mathbf{x}}_T(k) = \hat{\mathbf{x}}(k) + \mathbf{Z}(k)\mathbf{A}_p'[\mathbf{P}(k+1)]^{-1} \quad (17)$$

$$\times(\hat{\mathbf{x}}_T(k+1) - \hat{\mathbf{x}}(k+1)) \quad (18)$$

where $\hat{\mathbf{x}}_T$ represents the improved Kalman smoother estimates. A similar approach was used in [17].

IV. Simulation Results

Control and estimation schemes were tested in simulation to evaluate the relative importance of threshold sensing for microstage angular position estimation under various sampling and control settings. Basic observations on estimator performance are described in this section, while a discussion related to other calibration techniques is provided in Section VI. In numerical simulation, the threshold crossing is checked at each time instant of the regularly sampled (slow-sampled) plant dynamics. Whenever a threshold crossing is sensed, the threshold sensor loop is initiated using the actual states of the plant at the time instant just before the threshold crossing and exact crossing time is found by resimulating the time step in which crossing occurs at the fast threshold sampling rate. The regular Kalman filter estimates, which had been running at the same sampling rate as the plant, are then updated.

For simulation studies, the nominal second-order dynamics of the prototype actuator are taken to have a natural frequency of approximately 1.2 kHz and a damping ratio of 0.05. For simulation analysis, the range of deterministic disturbances is 5 Hz to 5 kHz with a maximum amplitude of 5% of the controlled input, and measurement noise was 17% of the signal amplitude, based on a capacitive sensing circuit model.

A. Velocity Estimation

Both sine wave and ramped-square reference signals have been tested in simulation. A sample steady-state response to a ramp input is shown in Fig. 3, in which the reference is a combination ramp and hold between 0° and 1°, or 0.018 rad. Using the analog and threshold sensors, measurements are taken which are used for estimating states at each time step. As noted previously, analog sensors are assumed to be noisy with Gaussian distribution, with potential error in their sensor gain (i.e., error in output matrix $\mathbf{C}_p$ of the state-space model), while threshold sensors are assumed to be placed at two locations between 0 and pi/180 rad.

Several features of Fig. 3 should be noted for explaining potential algorithm use in calibration. First, the system does not follow the reference trajectory very precisely. For calibration, it is more important to know the actual trajectory that was achieved, rather than achieving a specific target trajectory, though later in this section, use of feedback to make the actual trajectory more uniform will be seen to improve results. Second, additional accuracy provided by the threshold sensor in any given cycle is limited and highly variable due to noise. Thus, velocity estimates must be averaged over many cycles both to evaluate improvements in estimation and provide high-accuracy velocity estimation for calibration.

Thus, to evaluate estimator performance, angular velocity error at each time step in the excitation cycle is averaged over the cycles completed after reaching steady-state behavior. In simulation, 100 excitation cycles are performed, with average angular velocity error versus average angular velocity typically calculated for the last 20 time periods. For a sinusoidal input, this provides up to N_s possible angular velocity estimates for use in calibration, plus additional angular velocity estimates at the threshold detection instants. However, the average error at each angular velocity varies according to proximity to threshold detection events and error covariance variation over the excitation periods in the underlying Kalman filter.

To illustrate the importance of threshold sensing on average velocity estimation error at individual points in the cycle, Fig. 4 shows simulation results when two threshold sensors were hypothesized to be available at 0.2° and 0.65° (3.5 and 11.3 mrad). When using two threshold sensors, it is typically observed that two locations demonstrate a dramatically reduced angular rate error. Fig. 4 first shows

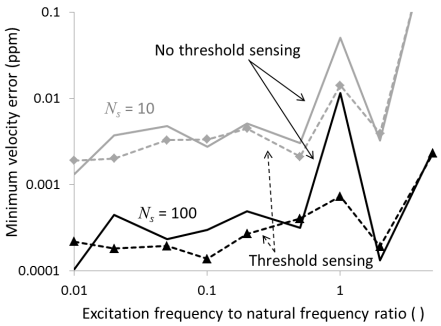

Fig. 5. Minimum relative velocity error shows improvement as sampling rates increase and threshold sensing is added; relative error plotted against (1) the ratio of input frequency to natural frequency; and (2) the ratio of fast sampling rate to slow sampling rate, averaged over 15 simulations each.

the mean velocity error at various angular positions for a sinusoidal reference and then shows the relative error at those locations as a function of angular velocity. Without threshold sensing, the velocity error is approximately 100 mrad/s, which decreases with threshold sensing to less than 10 mrad/s at certain positions, though the error can get worse at others. The corresponding relative angular rate error nearest the threshold locations reaches the order of 10^{-5}, although rate errors are largely unchanged or can even be made worse elsewhere in the cycle.

The angular velocities at which error is minimized are dependent on nominal dynamics, excitation frequency, sampling rates, and threshold angle locations. For a given disturbance range and noise variance, results are comparatively insensitive to disturbance and noise variation from simulation to simulation. This is advantageous for calibration tasks, as the set of estimated angular velocities to rely on during calibration can be predetermined. However, the precise positions at which velocity errors are minimized are not necessarily always exactly at the threshold angles, due to the comparatively slow sampling period of the primary sampling instants. When one of the threshold sensors is removed, the performance deteriorated and error value increased to the order 10^{-4}. For this case, the resulting errors are generally comparable with those in the capacitive-sensor-alone case. Much less improvement is to be expected due to the inability to effectively scale output measurements using threshold sensing information.

B. Sampling Effects

The best estimated velocity from a Kalman filter with and without a threshold sensor is highly dependent on both the actuation frequency and the slow (analog) and fast (clock) sensing frequencies. First, as the slow sampling rate decreases relative to the input frequency, estimator performance declines dramatically, though the change shown in Fig. 5 is likely overstated from a practical standpoint as sensor noise could likely be reduced for slower sampling rates. More importantly, as slow sampling rate decreases, threshold sensing benefits are reduced, as any additional information is less reliable by the next regular sampling instant.

With respect to excitation frequency, threshold sensing provides the greatest benefits when driving the actuator near its natural frequency. This is attributed to reduced relative disturbance influence when operating the piezoelectric stage near resonance. While this does not provide the absolute best angular velocity estimation errors, it is very useful as it is often necessary to operate MEMS actuators near resonance to obtain satisfactory motion amplitudes. Meanwhile, threshold sensing again provides little benefit when input frequencies are very low, and all estimation algorithms perform poorly above the stage's natural frequency as motion amplitudes drop off.

C. Feedback Control

Simulating the system response also allows various feedback controllers to be tested in conjunction with the three estimation schemes when the other nonideal disturbances, such as periodic vibration and hysteresis, are present in the system. The periodic nature of the reference trajectory is well suited to periodic control algorithms such as repetitive or iterative learning control (ILC). ILC is selected as the primary candidate control system to allow trajectory error from an entire cycle period to be used in the next (or a later) cycle, which is helpful for providing sufficient computation time to provide control at relatively high microactuator excitation frequencies.

The ILC technique chosen was a simple proportional gain, which will be shown to significantly improve estimation performance under certain circumstances. When the reference trajectory is a periodic signal

$$\mathbf{r}(t) = \mathbf{r}((t+T) = \mathbf{r}((t+N_s T_s) \tag{19}$$

where T is the period of the periodic reference and N_s is the number of slow samples per period, the control input is

$$u(N_s + k) = \mathbf{G}_{\mathrm{ILCT}} \times [\hat{\mathbf{x}}(k+1) - \mathbf{r}(k+1)] \tag{20}$$

where $\mathbf{G}_{\mathrm{ILCT}}$ is a proportional type ILC learning function and $\hat{\mathbf{x}}$ is the *a priori* state estimate.

To find the best learning function $\mathbf{G}_{\mathrm{ILCT}}$ of (20) for the nominal plant model, a grid-search of ILC gains over a wide range was performed, followed by a smaller numerical search between 10 and 200; gains less than 10 were found to converge too slowly, while gains greater than 200 led to instability. To select from within the smaller region of potential gains, the values producing minimum tracking error after the ILC gain had reached a steady-state value were selected from a simple brute force search. The typical convergence time was around 80 cycle periods. ILC input was initiated at zero in each simulation.

For further comparison, a PID controller was tuned manually for the same nominal plant, with best results from a potential difference (PD) controller with a proportional gain of 1200 and a derivative gain of 0.15, which improves both the settling time and the damping ratio of the system poles.

Both controllers are able to improve estimation accuracy at the highest accuracy estimation locations, especially when there is model uncertainty, as shown in Table I. This is attributed to their contribution to reducing cycle-to-cycle variation, either due to hysteresis and enduring disturbances with ILC or due to in-run random

TABLE I
CONSOLIDATED RESULTS FROM SIMULATION CASE STUDIES

Case		Best velocity error (ppm)	2nd best velocity error (ppm)	Implied scale error (ppm)
1	No control, perfect model	326	681	755
	with threshold sensing	218	520	564
2	No control, perturbed $\mathbf{C}$	3500	3800	5170
	with threshold sensing	390	850	935
3	With PD, perturbed $\mathbf{C}$	1180	1320	1770
	with threshold sensing	100	130	140
5	With ILC, perturbed $\mathbf{C}$	260	280	380
	with threshold sensing	40	70	80

disturbances with the PD control. For example, without ILC, perturbing the system model by altering the system's sensor gain without knowledge by the controller (Case 2 versus Case 1) produces almost an order of magnitude increase in estimation error without threshold sensing and approximately two-fold with threshold sensing. In contrast, when PD or ILC control is used, errors with and without perturbation are still reduced, though distributed differently between the most accurate velocity estimates (Case 3 and Case 4). In all cases, threshold sensing improves velocity estimation errors, though with greatest impact when estimation without threshold sensing is worst.

D. Estimated Calibration Accuracy

To evaluate potential gyroscope calibration errors using the best angular rate estimates, an error analysis is performed for a linear gyroscope assumed to have output

$$V_{\text{out}} = K\omega(t) + V_b \tag{21}$$

where V_{out} is the gyroscope output voltage, K is the true gyroscope gain, and V_b is the true gyroscope bias voltage. For a simple calibration scheme using two angular rate estimates, $\hat{\omega}_1$ and $\hat{\omega}_2$, to generate a gain estimate, $\hat{K}$, and $\hat{V}_b$

$$\hat{K} = \frac{V_{\text{out}}(\omega_1) - V_{\text{out}}(\omega_2)}{\hat{\omega}_1 - \hat{\omega}_2} \tag{22}$$

relative calibration error computed by root-mean-square methods becomes

$$\left|\frac{K - \hat{K}}{K}\right| \approx \left|\frac{\sqrt{e_{\omega_1}^2 + e_{\omega_2}^2}}{\omega_1 - \omega_2}\right| \tag{23}$$

where e_{ω_1} and e_{ω_2} are average angular velocities for the angular velocities selected for calibration.

Table I also shows projected calibration errors with the best angular rate estimates available using the various control and estimation schemes, for a sample candidate gyro [18] tested on a standard rate table having a nominal gain of 91 mV/rad/s and a bias of 1.35 V. Implied relative scale errors are on the order of 50–150 ppm when both ILC and threshold sensing are used, with some potential to further tune scale estimation error through proper selection of threshold locations (Case 5 in Table I). This is much better than the gyroscope's own gain or bias errors (worse than 10 000 ppm), and in best cases acceptable for gain errors in inertial gyroscopes [2], though implied bias errors are much larger.

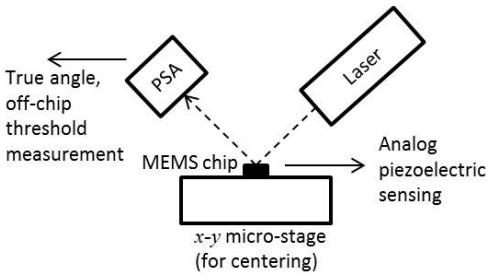

Fig. 6. For estimator testing with a prototype piezoelectric microactuator, off-chip laser detection is used to track true actuator rotation and insert threshold detection events into the motion-estimation algorithm.

V. EXPERIMENTAL RESULTS

To validate the proposed algorithm experimentally, a prototype piezoelectric stage was tested in rotational oscillation about its x-axis. The prototype stage was instrumented only with piezoelectric displacement sensing, rather than capacitive sensing, due to its production by an earlier fabrication process. As such, the stage lacked on-board threshold sensing. In its place, a helium–neon laser was reflected off the stage surface to a high-precision On-Trak light sensing array (LSA) translational sensor from which the angle is calculated geometrically. While the LSA is also subject to some drift over time, for estimator validation, the LSA response was treated as a true measurement of stage position, with two angles in the LSA measurement treated as threshold measurements. A schematic view of the experimental setup is shown in Fig. 6.

The reference LSA measurement trajectory used in the experimental verification of estimation algorithm was a sinusoidal signal of a frequency of 685 Hz and an amplitude of 3 V. This was obtained by applying an input voltage of amplitude of 1.5 V. A system model was identified using the circle fit method of modal analysis (natural frequency 678 Hz, damping ratio 1.8%, and gain 79 mdeg/V) from piezoelectric measurements and scaled to match the rotational amplitude measured by the LSA. During experimental tests, the piezoelectric sensor was sampled at approximately 20 kHz, while the LSA was sampled at approximately 35 kHz. LSA feedback is treated as perfect in the experimental study, though the true repeatability of the LSA at a maintained temperature in laboratory conditions is only approximately 100 ppm.

Figs. 7 and 8 compare the LSA output and threshold sensor algorithm estimates. The plot also indicates the threshold sensing points. During filtering, the threshold crossing improves the velocity estimates after the threshold sensing location, as is expected, and in smoothing it improves accuracy on both sides. Since the measurements for both filter and smoother are noisy,

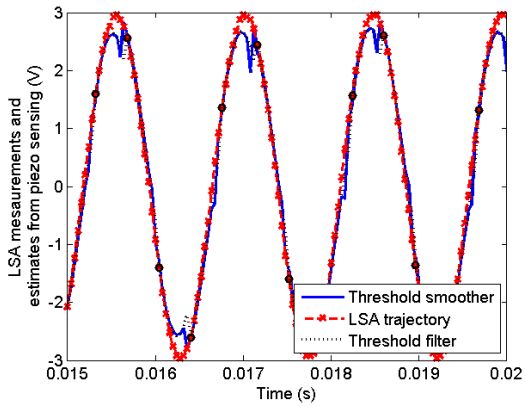

Fig. 7. Experimental verification of estimation algorithm shows close agreement between external LSA output and estimates based on a combination of on-board position sensing and select LSA threshold angles.

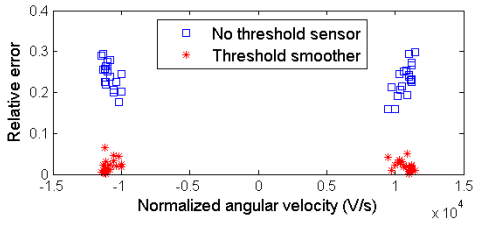

Fig. 8. Error in average velocity estimates calculated based on experimental results shows a substantial reduction when implementing threshold sensing.

a low-pass filter is used to filter out some of the high-frequency noise. The proposed algorithm estimates the derivative of the LSA output well near the threshold sensing points; while both piezoelectric and LSA angular measurements are less accurate than the capacitive sensing to be ultimately incorporated into the piezoelectric stage, substantial improvements in angular velocity error are seen, as listed in Table II. These errors range from 30% to 18% using piezoelectric sensing alone, versus approximately 5% to as low as 0.2% at maximum accuracy positions with threshold sensing. This improvement by a factor of 10 to 100 is consistent with improvements in simulation studies.

VI. Discussion

Table III shows the accuracy of a sample high-quality MEMS gyroscope, excitation stages, and gyroscope calibration techniques. The results presented for the velocity estimation in this brief may be most directly compared with other candidate excitation sources for gyroscope calibration. While velocity estimates for stage motion are much less accurate than precision rate tables, which can achieve errors of just 1 ppm, knowledge of piezoelectric stage motion at its highest accuracy is much better than that of a gyroscope on its own (noting again that the piezoelectric stage can again only deliver such accuracy at a finite set of velocities). Also shown for reference is a sample MEMS electromagnetic nanopositioning stage that also made use of detailed capacitive electrode modeling for high-accuracy position sensing, showing similar but somewhat less accuracy than that of the proposed scheme.

TABLE II
Error Coefficient Estimations Based on Experimental Results

	Best velocity error (ppm)	Second velocity error (ppm)	Implied scale error (ppm)
Without threshold	15600	17700	23600
With threshold	258	1340	1370

TABLE III
Comparison of Reported Stimulus and Gyroscope Calibration Accuracies. *Relative Accuracy Not Reported, Estimated From Reported Absolute Results

Method	Hardware added	Nominal rate (dps)	Best accuracy (ppm)
Gyroscope alone:			
ADIS16485	None		≈10,000
Stimulus alone:			
Proposed	MEMS piezo stage (sim)	300	80
	+ laser angle sensor (exp)	860	260
Laboratory [19]	Rate Table	≤1000	1
MEMS Stage [20]	MEMS EM stage	NA	430*
Scale calibration:			
Proposed	MEMS piezo stage (sim)	300	280
Continuous [7]	Gimballed gyro (sim)	0.004	1*
Multi+contin. [8]	Camera/tripod (sim)	Varied	100
	(experiment)	Varied	≈3000*
Multi-pos. [21]	Rate Table (ideal, sim)	0.01	0.1
Multi-pos. [22]	Rate Table (exp)	60	≈100
Multi-pos. [6]	100ppm Rate Table (exp)	1600	1000*
Multi-pos. [9]	Manually moved (exp)	0.004	4020
Self-cal. [4]	None (experiment)	5	350
	+feedback (experiment)	5	1
Self-cal. [3]	Temp. sensor	≤400	200

Once used in calibration, accuracy of gyroscope parameter estimates is generally not as good as that of the excitation stage. Although certain simulation studies have suggested accuracies to 1 ppm or better using high-accuracy rate tables or gimbaling techniques, practical calibration of low-cost (i.e., MEMS) gyroscopes is typically about an order of magnitude worse than the excitation accuracy. While the simulated calibration results presented here are better than that, they do not account for several nonidealities of MEMS gyroscopes. Still, even with substantially worse calibration results than predicted here, the piezoelectric microstage still offers a substantial improvement on a MEMS gyroscope alone, with much smaller hardware size, power, and time requirements than those of most proposed calibration methods.

The exceptions, however, are certain self-calibration techniques demonstrated in [3] and [4]. While highly design-specific to date, these efforts demonstrated MEMS gyroscope accuracy to just a few hundred parts per million from careful modeling of gyroscope response to perturbations and added stimulus within the gyroscope itself. Trusov *et al.* [4] further achieved a 1 ppm accuracy over 10 °C through use of feedback. The greatest opportunity of a microstage of the type presented here may be to generalize calibration to arbitrary, likely lower cost, microgyroscopes, though not to the degree possible for the most carefully modeled designs.

Practically, the biggest challenge for full implementation of this threshold sensing and estimation scheme is the need for threshold detection errors no worse than threshold timing clock resolution. While peak capacitance measurements can be demonstrated to be very stable, small capacitance still results in very small threshold sensing currents, which may make detection errors larger than assumed during simulation studies. Possible options for compensating would be the use of many threshold sensors or increasing the range-of-motion of the piezoelectric stage.

Beyond simply identifying a specific gyroscope gain (or bias), a microstage has mixed potential for addressing other nonideal gyroscope behaviors. The high speed at which calibration can be performed is a great advantage in avoiding error from intrinsic inertial sensor drift during the time required to run a calibration sequence. However, the limited number of velocities that can be known at the highest accuracy makes full characterization of nonlinearity in a gyroscope difficult. Finally, high-speed calibration requires any timing differences between gyroscope and stage sampling to be precisely known. The periodic excitation helps in synchronizing signals, and the threshold sensing scheme is designed to allow the asynchronous threshold crossing to inform estimates at the regular sampling instants, but for demanding inertial measurement applications, margin of error is small.

Finally, the proposed algorithm offers other benefits of a simple control structure and the ability to design for various criteria, likely with room for further improvement. Good results have been observed using very simple PD and ILC gain structures in simulation, but controller selection does affect estimator performance, and at present desirable gains are found only through a simple numerical search. Likewise, choice of threshold sensing locations and reference trajectory influences the angular velocities that are best estimated; these velocities are also currently identified only through simulation studies, with more rigorous prediction methods yet to be developed.

VII. Conclusion

A strategy for controlling a piezoelectric actuator to generate periodic reference trajectories for calibrating a MEMS gyroscope, as a method of improving MEMS IMU performance, has been presented. The chief contribution of the brief is to propose and evaluate through simulation and experimental studies the impact of incorporating a capacitive threshold sensor with conventional analog position sensing in the piezoelectric stage to substantially improve angular velocity estimation accuracy. Including threshold sensors reduced estimation errors by approximately 80% relative to a conventional Kalman filter, to as little as 20 ppm error in simulation studies. Feedback control is also observed to improve estimation accuracy in simulation. Experimentally, with less accurate piezoelectric and optical sensors available, the impact of threshold measurements was much greater, though best estimation accuracy was only 258 ppm. Relative to other calibration techniques, projected scale factor calibration may be competitive with existing field calibration techniques while being self-contained as a microscale system. Certain device specific self-calibration algorithms have demonstrated even greater accuracies, but also suggest that they can be further improved through use of motion stimulus.

As future work, angular velocity estimation will be tested on next-generation piezoelectric stages with capacitive sensing, currently being fabricated. It is expected that it will also be necessary to add additional axes of motion to control system design to account for nonidealities in microactuator behavior caused by cross-coupling between piezoelectric vibration modes in the various axes of motion. In addition, the interaction of ILC gain selection, threshold sensor positions, and resulting velocity estimate accuracy remains to be fully analyzed.

References

[1] J.-K. Shiau, C.-X. Huang, and M.-Y. Chang, "Noise characteristics of MEMS gyro's null drift and temperature compensation," *J. Appl. Sci. Eng.*, vol. 15, no. 3, pp. 239–246, 2012.

[2] M. Grewal and A. Andrews, "How good is your gyro?" *IEEE Control Syst. Mag.*, vol. 30, no. 1, pp. 12–86, Feb. 2010.

[3] A. Kourepenis, J. Borenstein, J. Connelly, R. Elliott, P. Ward, and M. Weinberg, "Performance of MEMS inertial sensors," in *Proc. IEEE Posit. Location Navigat. Symp.*, Apr. 1998, pp. 1–8.

[4] A. A. Trusov, I. P. Prikhodko, D. M. Rozelle, A. D. Meyer, and A. M. Shkel, "1 PPM precision self-calibration of scale factor in MEMS Coriolis vibratory gyroscopes," in *Proc. 17th Int. Conf. Solid-State Sensors, Actuat. Microsyst.*, Jun. 2013, pp. 2531–2534.

[5] Z. F. Syed, P. Aggarwal, C. Goodall, X. Niu, and N. El-Sheimy, "A new multi-position calibration method for MEMS inertial navigation systems," *Meas. Sci. Technol.*, vol. 18, no. 7, pp. 1897–1907, 2006.

[6] J. K. Bekkeng, "Calibration of a novel MEMS inertial reference unit," *IEEE Trans. Instrum. Meas.*, vol. 58, no. 6, pp. 1967–1974, Jun. 2009.

[7] Y. Cao, H. Cai, S. Zhang, and A. Li, "A new continuous self-calibration scheme for a gimbaled inertial measurement unit," *Meas. Sci. Technol.*, vol. 23, no. 1, p. 015103, 2012.

[8] M. Hwangbo, J.-S. Kim, and T. Kanada, "IMU self-calibration using factorization," *IEEE Trans. Robot.*, vol. 29, no. 2, pp. 493–507, Apr. 2013.

[9] D. Teldadi, A. Pretto, and E. Menegatti, "A robust and easy to implement method for IMU calibration without external equipments," in *Proc. IEEE Int. Conf. Robot. Autom.*, May/Jun. 2014, pp. 3042–3049.

[10] E. E. Aktakka, R. L. Peterson, and K. Najafi, "A 3-DOF piezoelectric micro vibratory stage based on bulk-PZT/silicon crab-leg suspensions," in *Proc. 26th IEEE Int. Conf. Micro Electro Mech. Syst. (MEMS)*, Taipei, Taiwan, Jan. 2013, pp. 576–579.

[11] J. Astrom, *Analysis and Design of Nonlinear Control Systems*. Berlin, Germany: Springer-Verlag, 2008.

[12] M. Lemmon. (2010). *Lectures of the 3rd WIDE Summer School on Networked Control Systems*. [Online]. Available: http://www.nd.edu/lemmon

[13] X. Wang and M. D. Lemmon, "Event-triggering in distributed networked control systems," *IEEE Trans. Autom. Control*, vol. 56, no. 3, pp. 586–601, Mar. 2011.

[14] K. W. Verkerk, J. Achterberg, C. M. M. van Lierop, and S. Weiland, "Modal observer design for a flexible motion system with state dependent sensor positions," in *Proc. IEEE 51st Annu. Conf. Decision Control (CDC)*, Dec. 2012, pp. 4498–4504.

[15] D. Spinello and D. J. Stilwell, "Nonlinear estimation with state-dependent Gaussian observation noise," *IEEE Trans. Autom. Control*, vol. 55, no. 6, pp. 1358–1366, Jun. 2010.

[16] B. Edamana and K. R. Oldham, "A near-optimal sensor scheduling strategy for an on–off controller with an expensive sensor," *IEEE/ASME Trans. Mechatronics*, vol. 19, no. 1, pp. 158–170, Feb. 2014.

[17] C.-C. Wang and M. Tomizuka, "Iterative learning control of mechanical systems with slow sampling rate position measurements," in *Proc. ASME Dyn. Syst. Control Conf. (DSCC)*, 2008, pp. 1261–1267.

[18] *ISZ-505 Single-Axis Z-Gyro Product Specification*, Invensense, San Jose, CA, USA, 2011, pp. 1–27. [Online]. Available: http://www.invensense.com

[19] Ideal Aerosmith, Inc. *2001P Series Single-Axis Precision Positioning and Rate Table System*. [Online]. Available: http://www.ideal-aerosmith.com, accessed Jul. 25, 2014.

[20] J.-L. Lee, X. Huang, and P. B. Chu, "Nanoprecision MEMS capacitive sensor for linear and rotational positioning," *J. Microelectromech. Syst.*, vol. 18, no. 3, pp. 660–670, Jun. 2009.

[21] B. Fang, W. Chou, and L. Ding, "An optimal calibration method for a MEMS inertial measurement unit," *Int. J. Adv. Robot. Syst.*, vol. 11, no. 14, p. 57516, 2014.

[22] Sentera Technology. *MEMS IMU Calibration Example*. [Online]. Available: http://www.motionsense.com, accessed Jul. 24, 2014.